IOP Publishing Journal of Physics D: Applied Physics

J. Phys. D: Appl. Phys. **51** (2018) 145202 (8pp) https://doi.org/10.1088/1361-6463/aab1ac

Secondary electron emission from textured surfaces

C E Huerta, M I Patino and R E Wirz

University of California, Los Angeles, CA 90095, United States of America

E-mail: ceshuer@g.ucla.edu

Received 27 September 2017, revised 13 February 2018
Accepted for publication 22 February 2018
Published 13 March 2018

Abstract

In this work, a Monte Carlo model is used to investigate electron induced secondary electron emission for varying effects of complex surfaces by using simple geometric constructs. Geometries used in the model include: vertical fibers for velvet-like surfaces, tapered pillars for carpet-like surfaces, and a cage-like configuration of interlaced horizontal and vertical fibers for nano-structured fuzz. The model accurately captures the secondary electron emission yield dependence on incidence angle. The model shows that unlike other structured surfaces previously studied, tungsten fuzz exhibits secondary electron emission yield that is independent of primary electron incidence angle, due to the prevalence of horizontally-oriented fibers in the fuzz geometry. This is confirmed with new data presented herein of the secondary electron emission yield of tungsten fuzz at incidence angles from 0–60°.

Keywords: plasma-material interactions, secondary electron emission, surface texturing

(Some figures may appear in colour only in the online journal)

1. Introduction

Secondary electron emission (SEE) affects the performance of plasma devices for a wide range of energies and applications such as fusion [1–3], plasma processing [4, 5], and electric propulsion [6–9]. Because SEE leads to a reduction in the sheath potential, wall heat losses increase and the energy of electrons in the plasma bulk decreases as high energy electrons are absorbed by the walls and low energy secondary electrons are emitted back [10]. In tokamaks, for instance, SEE increases the heat transmission to the wall and releases cold electrons into the scrape-off layer [2, 11].

Textured surfaces have been shown experimentally [12–14] and computationally [15, 16] to suppress SEE by capturing emitted and backscattered secondary electrons. This suppression is due to geometric effects and can also be observed in sputtering of featured surfaces exposed to plasma [17–19]. In electric propulsion devices, carbon velvet has been used to improve performance; a similar effect could be realized in fusion devices via surface fuzz formation at the divertor plate. Recently, tungsten fuzz has generated interest due to its natural occurrence under tokamak disturbance-like conditions [20–24], which could allow for the sustained reduction of SEE (as opposed to conventional manufactured surfaces, where features gradually erode away). A similar reduction in the yield has also been measured for ion-induced SEE from tungsten fuzz [25].

Computational and analytical efforts have been previously used to understand the observed reduction in yield due to surface texturing. Pivi *et al* [13] simulated surface grooves through Monte Carlo particle pushing and predicted a reduction in the SEE yield which agreed with experimental measurements of similarly textured samples. Similarly, Ye *et al* [26] simulated surfaces with pore arrays and obtained complex, nonmonotonic dependencies between yield and incident angle for various pore configurations. More recently, Swanson and Kaganovich [16] compared particle pushing model results with analytical derivations of the reduction in yield due to vertical pillars protruding from a substrate. Despite the success of previous efforts, complex surface geometries such as fuzz and carpet surfaces have not been simulated.

The objective of this work is to show that simple, repeating geometries can accurately and efficiently model SEE behavior of textured surfaces (see figure 1). Most notably, we demonstrate that a simple cage-like geometry can be used to accurately simulate the SEE behavior for nano-structured tungsten fuzz. Modeling results are compared with computational and analytical results, as well as both historical and recent yield

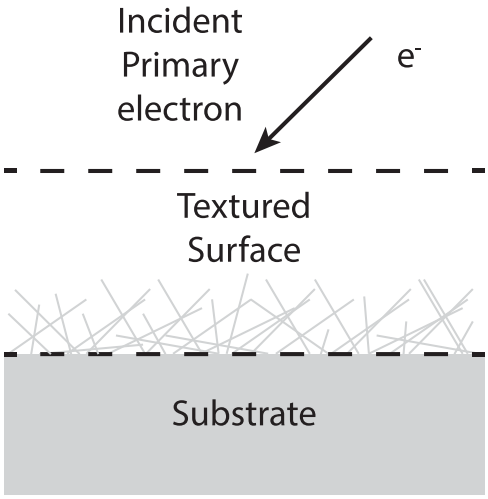

Figure 1. Regions defined by computational model. The focus of this work is to accurately and efficiently model a representative geometry for textured surfaces.

measurements, capturing distinct effects of the surface morphology on SEE and its dependence on incident angle. Along with the modeling results, new measurements are presented which show that tungsten fuzz greatly affects SEE yield and angular dependence.

2. Computational approach

The model simulates the interactions of incident primary electrons with the surface, and hence requires knowledge of material SEE properties, surface geometry, and electron incidence conditions (energy and angle). This work focuses on accurately modeling textured surfaces to examine surface texturing effects on the SEE yield behavior (see figure 1). The following subsections detail the particle tracking, collisional and emission behavior, and geometric components of the model.

2.1. Electron tracking

The model uses a Monte Carlo approach to push primary electrons towards the surface and then simulates the SEE behavior when a collision with the material is detected (see figure 2). Because the typical Debye length of plasma devices of interest (EP and fusion devices) is larger than the surface layer, the electric and magnetic fields are assumed to be negligible near the surface. For example, for tokamaks, the Debye length is on the order of 10^{-4} m [27], while the surface layer (length of vertical fibers) is on the order of 100 nm–1 μm. Hence, electrons travel linearly until colliding with a surface. In addition, primary and secondary electrons have mean free paths much larger than the surface feature scales, so their velocities change only after colliding with a surface.

At the low energies investigated herein, electron penetration depth into metals approaches a few nanometers and is therefore neglected. As primary electrons penetrate the surface, they collide with electrons to generate true secondary electrons or are inelastically backscattered, usually a small

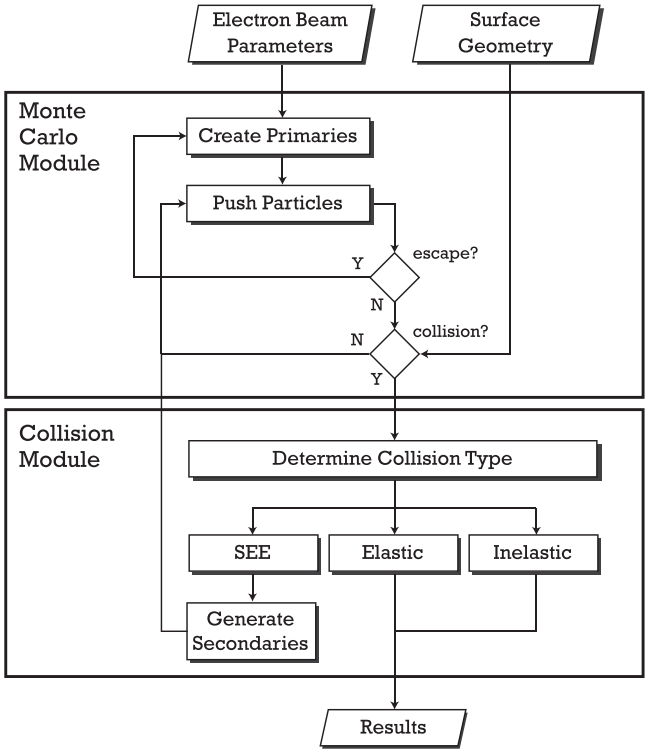

Figure 2. Flow chart for SEE model.

distance away from the point of collision. For the simulated conditions, this distance is small relative to fiber dimensions (for the worst case, primary electron penetration depth for tungsten is ~5 nm at normal incidence, compared to the 200 nm computational domain length) so inelastically backscattered and true secondary electrons are assumed to be emitted from the point of impact (see figures 3(c) and (d)). Moreover, although primary electrons can inelastically backscatter while also generating true secondary electrons (see figure 3(a)), in this model, incident electrons are assumed to be lost (or absorbed) when true secondary electrons are generated.

Primary electrons are seeded at the top face some distance above the fiber tops and secondary electrons are only allowed to escape through this boundary. Electrons are reflected from the lateral boundaries (since the computational domain repeats infinitely in the lateral directions) and retained until they escape or are absorbed. Electrons are pushed linearly until a collision is detected geometrically by the intersection of the electron's path segment and a fiber cylinder or the substrate plane.

Using empirical fits from Tolias [28] and de Lara *et al* [29], a probabilistic model backscatters the primary electrons (elastically or inelastically) or removes them and generates a randomly calculated number of true secondary electrons (see section 2.2). These backscattered and true secondary electrons are then tracked through further collisions or until escaping through the top boundary of the computational domain. The algorithm limits the number of further secondary generations to two since additional generations were observed to negligibly affect the calculated true secondary yield in early runs of the model.

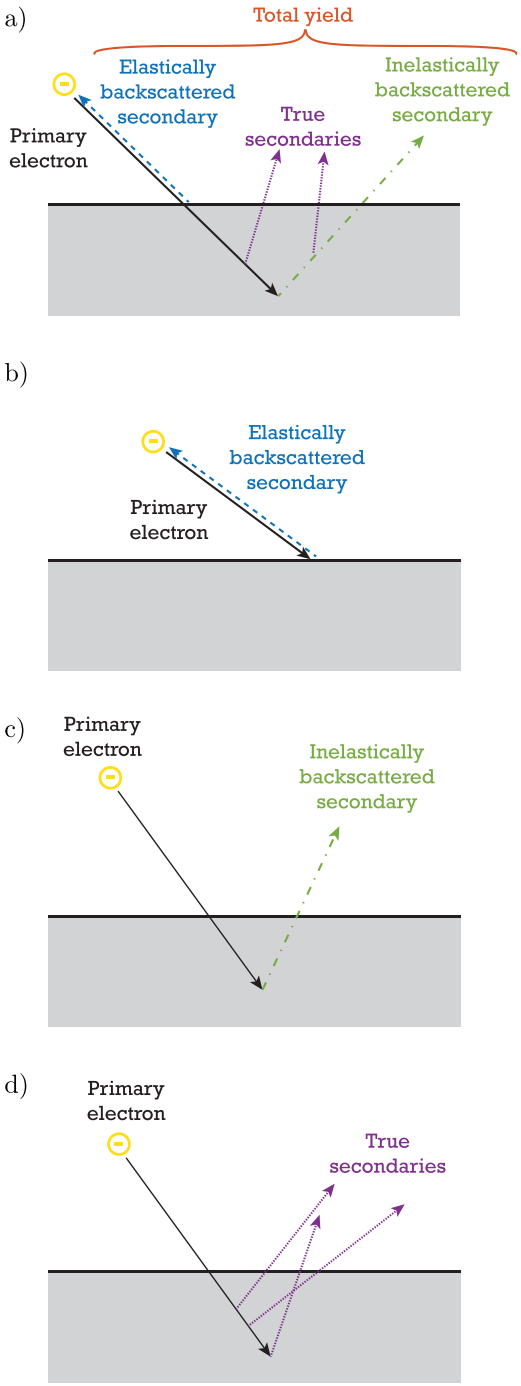

Figure 3. (a) Secondary electron emission events. Inelastic backscattering and true secondary emission are not mutually exclusive, but are separated in this model. (b) Elastic backscattering. (c) Inelastic backscattering. Inelastically backscattered secondary electrons are reflected from the point of collision and do not generate true secondary electrons in this model. (d) True secondary generation. True secondary electrons are assumed to be generated at the point of collision.

2.2. Secondary electron emission treatment

Surfaces impacted by primary electrons emit secondary electrons through three different processes: elastic and inelastic backscattering, and true secondary emission, as shown in figure 3. Elastically backscattered secondary electrons are reflected at the surface and retain their pre-impact energy. Inelastically backscattered secondary electrons, on the other hand, penetrate the surface and lose some energy before recoiling away from the surface. Finally, true secondary electrons are emitted due to collisions between primary electrons and near-surface atoms within the bulk. The respective yields for each type of secondary electrons are ε and η for elastic and inelastic backscattering and δ for true secondary electrons, and represent the ratio of the flux of each type of secondary to the flux of primary electrons. Each secondary population is treated independently in this model.

2.2.1. Backscattered secondary electrons. Jonker [30] has previously measured the angular distribution of 'rapid' backscattered secondary electrons emitted from nickel at several incident energies and angles, showing that these secondary electrons are reflected preferentially at near incidence angles. The spread in these distributions is likely due to the inclusion of inelastically backscattered secondary electrons and is neglected. Elastic backscattering is therefore modeled by retaining the electron's incident energy (E_i) and reflecting the particle back through its original trajectory as shown in figure 3.

For inelastically backscattered secondary electrons, a uniform energy distribution in the range $50\ \text{eV} < E_{\text{SE}} < E_i$ is assumed. Jonker's measured angular distributions for these secondary electrons are nearly cosine, with a slight bias toward the incidence angle. For simplicity, a cosine emission distribution is used.

A probabilistic model developed by de Lara *et al* [29] is modified using Tolias' empirical fits [28] to SEE yield data taken at low incident energies by El Gomati *et al* [31]. This modification corrects the backscattering yield behavior to monotonically decrease at low incident energies, as discussed in [32]. The modified inelastic and elastic backscattering probabilities thus become:

$$\begin{aligned}
\eta(E_i) &= a\,(1 - b\,E_i)\,{E_i}^{\gamma}\,\exp\left(-\left(\frac{E_i}{c + \mathrm{d}Z}\right)^{\mu}\right)\\
\varepsilon(E_i) &= f\,(1 - \mathrm{e}^{-gE_i}) - \eta(E_i)\\
\eta(E_i, \theta_i) &= \eta(E_i)^{\cos\theta_i}\left(0.89\,\frac{\eta(E_i)}{\varepsilon(E_i) + \eta(E_i)}\right)^{1-\cos\theta_i}\\
\varepsilon(E_i, \theta_i) &= \varepsilon(E_i)^{\cos\theta_i}
\end{aligned} \tag{1}$$

where E_i and θ_i are the incident energy and angle and Z is the surface atomic mass number. The other parameters, a, b, c, d, f, g, γ, and μ, are fit values which can be found in [29] for η and [28] for ε. Each primary electron is backscattered as a single secondary, so the probability of backscattering is equal to the yield. Hence, a random number generator is used to determine what type of secondary is emitted after each collision (note that the probability of true secondary emission is $1 - \eta - \varepsilon$) [29].

2.2.2. True secondary electrons. For consistency, the true secondary model presented by de Lara *et al* is used [29]:

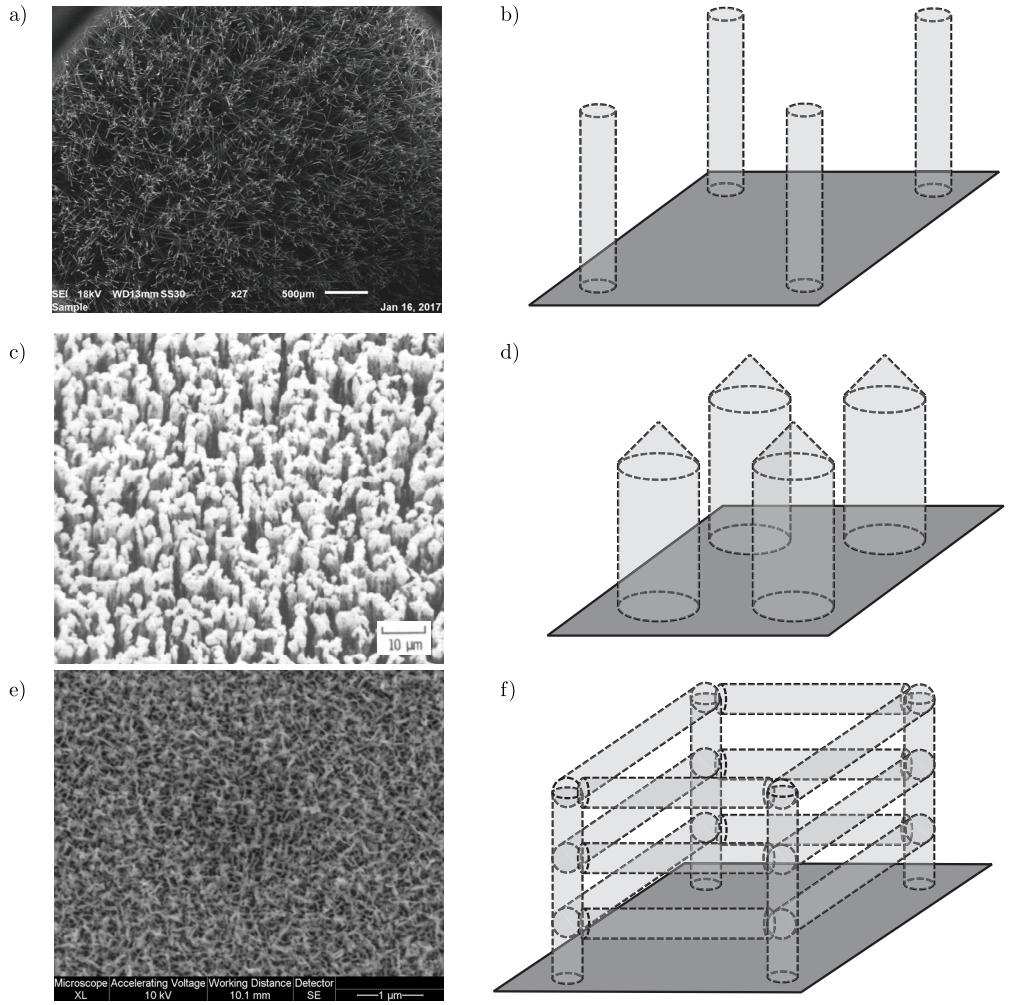

Figure 4. (a) Carbon velvet scanning electron microscope (SEM) image. (b) Pillar geometry and computational domain. (c) Copper carpet SEM image, reproduced from [36]. (d) Tapered fiber geometry and computational domain. (e) Tungsten fuzz SEM image. (f) Cage-like geometry and computational domain. Note: computational domains are representative and not to scale. See tables 1 and 2 for dimensions.

$$\begin{aligned}\delta(E_i) &= \delta_m \frac{s\,\frac{E_i}{E_m}}{s-1+\left(\frac{E_i}{E_m}\right)^s}\\ \delta(E_i,\theta_i) &= \delta(E_i)\,\frac{k+1}{k+\cos\theta_i}\\ k &= 0.0027\,Z + r.\end{aligned} \tag{2}$$

Here, δ_m is the maximum true yield, E_m is the incident energy at which δ_m occurs, s is a material-dependent parameter, and r accounts for surface smoothness [29]. These parameters can be obtained for specific surfaces by curve-fitting to experimental yield data from flat, clean samples.

When a collision results in the emission of true secondary electrons (with probability $1-\varepsilon-\eta$), the probability that n secondary electrons are emitted is calculated using a Poisson distribution such that the average number of secondary electrons emitted for all collisions equals the true secondary yield:

$$\begin{aligned}P_n &= \frac{\lambda^n \exp(-\lambda)}{n!}\\ \lambda &= \frac{\delta}{(1-\varepsilon-\eta)}\end{aligned} \tag{3}$$

where $n = 0, 1, 2, \ldots$ is the number of true secondary electrons generated and λ is the average number of true secondary electrons generated per impact [29, 33]. Each true secondary is assumed to be generated at the point of impact and follows a cosine angular distribution of emission independent of incident angle and energy [33, 34] and an energy distribution given by

$$f(E_{\mathrm{SE}}) = \frac{E_{\mathrm{SE}}}{(E_{\mathrm{SE}}+W_f)^4} \tag{4}$$

where W_f is the material's work function [34, 35].

Elastically backscattered, inelastically backscattered, and true secondary electrons can be distinguished experimentally using an energy analyzer (e.g. gridded retarding potential analyzer, hemispherical energy analyzer, or cylindrical mirror analyzer). However, many SEE measuring facilities often lack such energy analyzers due to their complexity and cost.

2.3. Geometry

To examine what type of simple repeating geometry can be used to accurately and efficiently simulate the SEE behavior

for the complex, chaotic geometry of velvet/carpet/fuzz, we utilized three different geometries, as shown on figure 4. A repeating, rectangular 3D section of the textured surface layer is used as the computational domain. The bottom face is treated as the solid, underlying substrate, and cylindrical fibers are positioned (in various configurations) at the corners of the domain. Three different geometries are employed to model different textured surfaces in this work:

– A repeating lattice of vertical, cylindrical whiskers, analogous to carbon velvet, which is similar to the geometry used by Swanson and Kaganovich [16].
– A copper carpet, tested by Curren *et al* [12], is modeled as vertical cylindrical fibers with low aspect ratio and tapered tops, centered at the corners of the substrate.
– A plasma-generated tungsten fuzz, which Patino *et al* studied in [14], is modeled as cylindrical fibers located at the substrate corners and connected by evenly distributed horizontal fibers in a cage-like geometry.

Figure 4 shows scanning electron microscope (SEM) images of the experimentally tested samples, as well as diagrams of the pillar, tapered fiber, and cage geometries used to model them.

3. Results and discussion

Simulation results of the SEE yield were compared with measured and computed yields from various textured samples. The first is a carbon velvet modeled by Swanson and Kaganovich [16]; the second an ion-textured, oxygen-free, high-conductivity copper carpet from [12]; and the third a tungsten fuzz sample (see [14]) prepared at the MIT Plasma Science and Fusion Center, which occurs naturally when a heated tungsten surface (>1000 K) is exposed to helium plasma with ion energies >10 eV and fluxes $>10^{20}$ m^{-2} s^{-1} (these conditions may occur in tokamaks that use tungsten as a plasma facing material).

3.1. Carbon velvet

To directly compare with Swanson and Kaganovich's model, the total SEE yield was modeled as:

$$\gamma(E_i,\theta_i) = \gamma_{\max}(\theta_i)\ \exp\left[-\left(\frac{\ln\left[E_i/E_{\max}(\theta_i)\right]}{\sqrt{(2)}\sigma}\right)^2\right]$$

$$E_{\max}(\theta_i) = E_{\max_0}\left(1+\frac{k_s\theta_i^2}{\pi}\right)$$

$$\gamma_{\max}(\theta_i) = \gamma_{\max_0}\left(1+\frac{k_s\theta_i^2}{2\pi}\right). \quad (5)$$

The backscattering yields were obtained by multiplying the total yield by the fraction of elastically and inelastically backscattered secondary electrons as given in [16]. In addition, all secondary electrons were reflected with a cosine distribution, inelastically backscattered secondary electrons have a 0 eV – E_i uniform energy distribution, and true secondary electrons were emitted with a Maxwellian energy distribution with $T = 5.4$ eV.

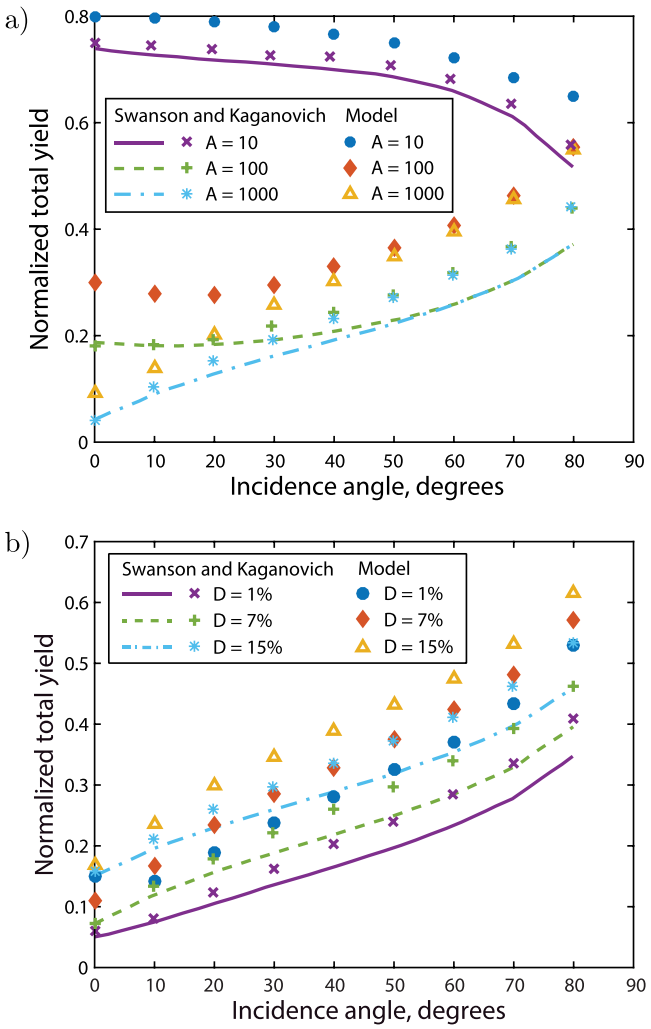

Figure 5. True secondary yield results from pillar geometry, compared with computational (symbols) and analytical (lines) results from Swanson and Kaganovich [16] for varying (a) aspect ratios and (b) packing densities.

As shown in figure 5, the computed yield agrees well with analytical and simulation results from Swanson and Kaganovich for varying fiber aspect ratio ($A = h/r$) and packing density ($D = \pi r^2/s^2$). For these simulations, the fiber radius, r, was kept constant while the fiber height, h, and separation distance, s, were changed. The models agreed especially well when the aspect ratio and packing density were high. Most of the difference was likely due to the different approaches of each model; instead of using Monte Carlo to backscatter and emit secondary electrons, Swanson and Kaganovich [16] tracked weighted macroparticles and changed their weight after each collision according to the total yield. Moreover, collisions in their model were detected using isosurfaces which coincide with the fibers rather than geometrically detecting the intersection of the particle's path with a surface. The analytical results are known to underestimate the yield because they do not account for tertiary electrons emitted by secondary electrons or the energy distributions of each type of emitted secondary electrons. Nevertheless, our

Table 1. Copper carpet fiber dimensions from [12] and from estimates of the SEM images.

Fiber radius	350 nm
Fiber length	1500 nm
Fiber separation	1000 nm
Tip taper angle	45°

model was capable of capturing the reversal of yield dependence on incidence angle as the aspect ratio increases past 100, which was analytically explained in [16].

3.2. Copper carpet

The tapered fiber geometry closely resembles a repeating section of the copper carpet, as shown in figure 4. From the carpet image, we estimated an average taper angle (i.e. the angle between the fiber tip surface normal and the fiber axis) of 45°, however, we examined the effects of this taper angle on the SEE results from the model. Measurements from the SEM image of the surface, along with estimates reported by Curren *et al* [12] are summarized in table 1. The material-dependent fit values for copper were obtained by fitting to their flat copper data (see figure 6(a)). Figure 6(b) shows the true secondary electron yield from the carpet sample at 0° and 45° incidence angles for a 200–2000 eV energy range. In general, the computational results agree well with the trends and magnitudes from the experimental data, especially considering that roughening of fiber and substrate surfaces or changes in chemical composition during the fabrication process was not considered.

Because of the uncertainty in the taper angle estimates, a parametric study was carried out to gauge the effects of fiber tip tapering. These results are shown on figure 6(c) for a constant incident energy of 200 eV and normalized by the true secondary yield from flat copper. This highlights the importance of accounting for fiber tapering in accurately modeling this particular textured surface. For example, flat-top fibers (0° taper angle) increase the SEE yield by ∼25%–40% as compared with 45° tapered fibers. Moreover, changing the taper angle by $\sim \pm 10°$ from 45° affects the results by less than 4%, so precisely estimating the taper angle is not necessary in this range.

Although the true secondary yield at 45° incidence was almost 40% higher than at normal incidence for a flat copper surface (see equation (2), the fiber tips funneled electrons toward the substrate, resulting in increased trapping of secondary electrons and a reduction in the calculated/measured yield. These competing effects are evident in the non-monotonic trend of figure 6(c): as the fiber taper angle was increased, more backscattered secondary electrons were channeled to the substrate, reducing the yield up to a minimum at about 25°. Increasing the taper angle further resulted in an increase in escaped secondary electrons because of the local increase in yield at the fiber tips (and because the tapered section of the fiber constitutes a larger fraction of the fiber in order to keep

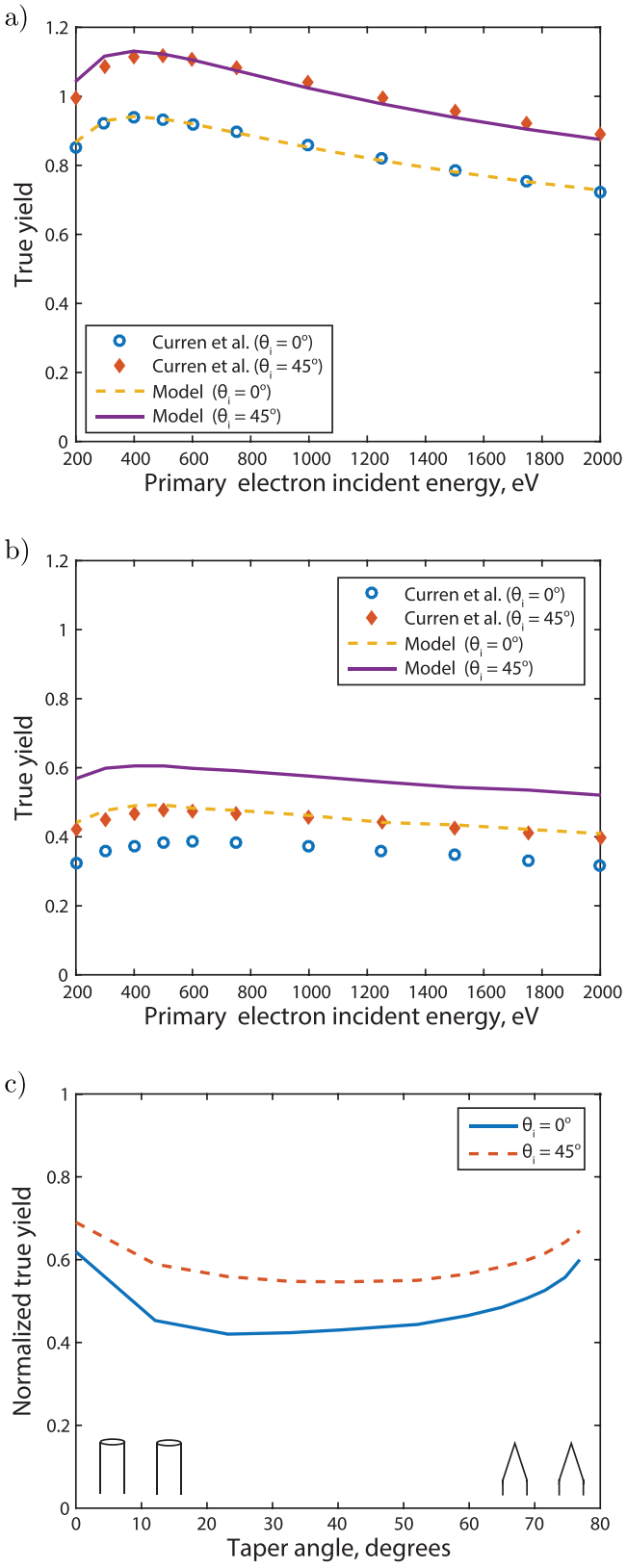

Figure 6. (a) True secondary yield from flat copper, compared with data from Curren *et al* [12]. (b) Comparison of true secondary yield results from tapered fiber geometry with copper carpet data. (c) Results from parametric study of taper angle (angle between fiber axis and tip surface normal).

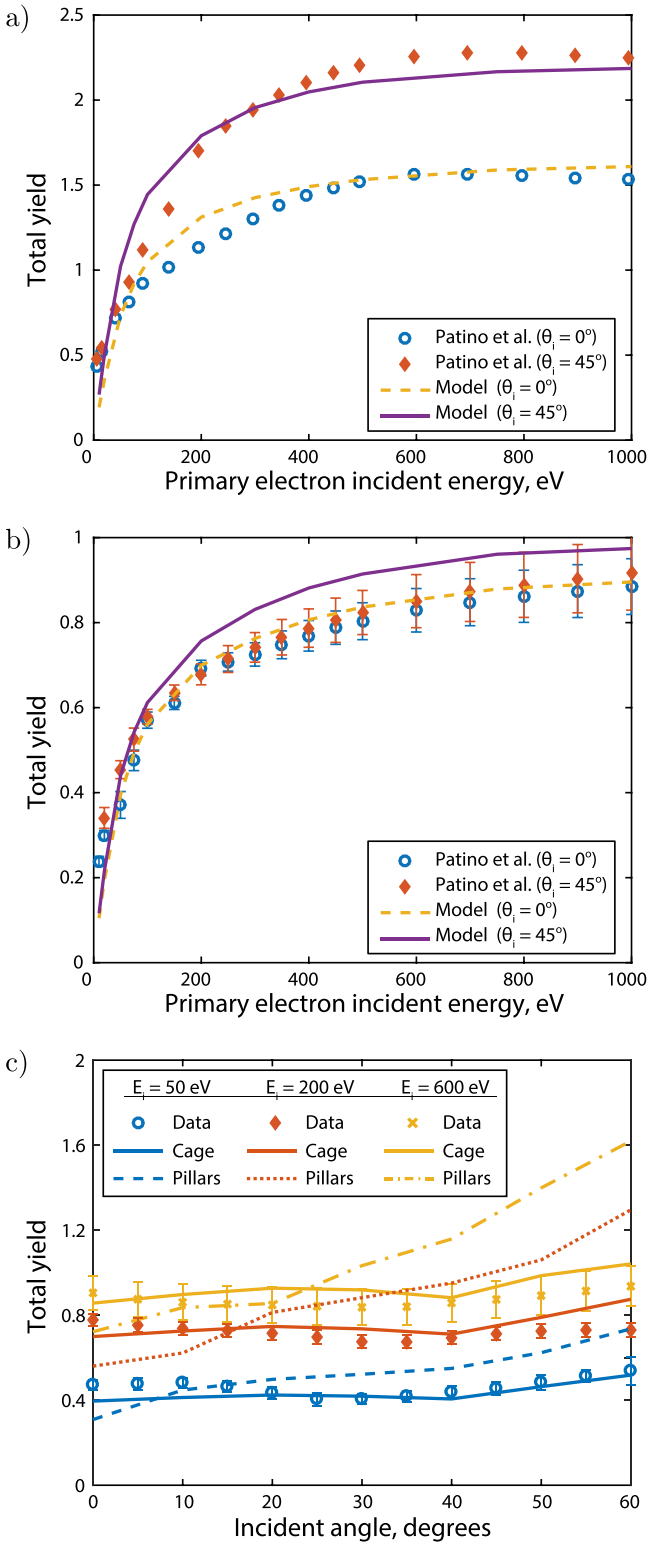

Figure 7. (a) Total secondary yield from flat tungsten. Computational results of total secondary electron yield dependence on (b) incident energy and (c) incident angle for tungsten fuzz, with (cage) and without (pillars) horizontal fibers, in the latter case. Experimental data in (a) and (b) are reproduced from Patino *et al* [14].

the radius and length constant). These effects were seen at both 0° and 45° incidence angles, although at normal incidence, the decrease in yield was more noticeable.

Table 2. Tungsten fuzz fiber dimensions measured from SEM images.

Fiber radius	12.5 nm
Fiber length	200 nm
Fiber separation	200 nm
Horizontal fibers	5 Per side

3.3. Tungsten fuzz

To examine nano-structured surfaces, the model was compared with recent experimental measurements of the yield from a well-characterized tungsten fuzz sample. Data in figures 7(a) and (b) were taken from [14]. The data shown on figure 7(c) are new (taken using the methods described in [14]) and show the yield from nano-structured fuzz for primary electron incident angles of 0–60°. This fuzz exhibits both vertical and horizontal fibers intertwined throughout the surface, so a cage-like geometry was used in our simulations. Table 2 summarizes the fiber dimensions measured from SEM images and figure 7(a) shows curve fitting to flat tungsten yield data.

Comparing the fuzz results with experimental measurements shows good agreement in both trend and magnitude generally within the experimental error (see figure 7(b)). Experimental data (see figure 7(c)) shows that the yield is nearly constant across all incident angles. The results show that this behavior is due to increased trapping of secondary electrons by the horizontal fibers; when the fuzz is modeled using vertical pillars only, there is a monotonic increase in the yield with increasing incidence angle. In addition, omission of the horizontal fibers in the model results in sharp disagreements with the data.

4. Conclusion

The results of this work show that the behavior of SEE from several common textured surface geometries can be accurately and efficiently modeled with relatively simple geometric constructs. Results were compared to and agreed with calculated and measured yield data from geometrically dissimilar carbon velvet, copper carpet, and tungsten fuzz surfaces, as well as new data of the independence of yield on incidence angle for tungsten fuzz presented in this paper. Most importantly, the model captured contrasting surface effects on the yield's dependence on incidence angle between the different surface configurations via geometric modifications, showing its flexibility in simulating textured surface SEE. The model was able to simulate the reversal in the yield's dependence on incidence angle as the fiber aspect ratio increased past 100 for velvet geometries and the critical effect of fiber tip taper angle for carpet geometries. A very important result of this study was based on new data, which show that yield is independent of all incident angles for nano-structured fuzz geometries. This behavior is unique in comparison to many other textured surfaces. Our simulations show that this angular independence is primarily due to trapping of secondary electrons by the horizontally-oriented fibers in such a geometry. Future work is of interest for surfaces with similar geometric features, such as foam.

Acknowledgments

The authors would like to acknowledge Dr Yevgeny Raitses for his assistance with the experimental measurements. This work is funded by AFOSR Grant No. FA9550-14-10317, DOE Office of Science Graduate Student Research Program, the University of California Eugene V Cota-Robles Fellowship, and by the UCLA School of Engineering and Applied Sciences.

ORCID iDs

C E Huerta https://orcid.org/0000-0001-7159-9995

References

[1] Farhang H, Napchan E and Blott B 1993 Electron backscattering and secondary electron emission from carbon targets: comparison of experimental results with Monte Carlo simulations *J. Phys. D: Appl. Phys.* **26** 2266
[2] Gunn J 2012 Evidence for strong secondary electron emission in the tokamak scrape-off layer *Plasma Phys. Control. Fusion* **54** 085007
[3] Lee W and Krasheninnikov S 2013 Secondary electron emission and the bifurcation of the heat flux to the targets in fusion plasmas *Phys. Plasmas* **20** 122501
[4] Perry A, Vender D and Boswell R 1991 The application of the helicon source to plasma processing *J. Vac. Sci. Technol.* B **9** 310–7
[5] Goree J 1994 Charging of particles in a plasma *Plasma Sources Sci. Technol.* **3** 400
[6] Raitses Y, Kaganovich I, Khrabrov A, Sydorenko D, Fisch N and Smolyakov A 2011 Effect of secondary electron emission on electron cross-field current in discharges *IEEE Trans. Plasma Sci.* **39** 995–1006
[7] Sydorenko D, Smolyakov A, Kaganovich I and Raitses Y 2008 Plasma-sheath instability in Hall thrusters due to periodic modulation of the energy of secondary electrons in cyclotron motion *Phys. Plasmas* **15** 053506
[8] Dunaevsky A, Raitses Y and Fisch N 2003 Secondary electron emission from dielectric materials of a Hall thruster with segmented electrodes *Phys. Plasmas* **10** 2574–7
[9] Sydorenko D, Smolyakov A, Kaganovich I and Raitses Y 2006 Kinetic simulation of secondary electron emission effects in Hall thrusters *Phys. Plasmas* **13** 014501
[10] Hobbs G and Wesson J 1967 Heat flow through a Langmuir sheath in the presence of electron emission *Plasma Phys.* **9** 85
[11] Stangeby P 1984 Plasma sheath transmission factors for tokamak edge plasmas *Phys. Fluids* **27** 682–90
[12] Curren A, Jensen K and Roman R 1990 Secondary electron emission characteristics of molybdenum-masked, ion-textured OFHC copper *Technical Report* NASA
[13] Pivi M, King F, Kirby R, Raubenheimer T, Stupakov G and Le Pimpec F 2008 Sharp reduction of the secondary electron emission yield from grooved surfaces *J. Appl. Phys.* **104** 104904
[14] Patino M, Raitses Y and Wirz R 2016 Secondary electron emission from plasma-generated nanostructured tungsten fuzz *Appl. Phys. Lett.* **109** 201602
[15] Huerta C and Wirz R 2016 Surface geometry effects on secondary electron emission via Monte Carlo modeling *52nd AIAA/SAE/ASEE Joint Propulsion Conf.* p 4840
[16] Swanson C and Kaganovich I 2016 Modeling of reduced effective secondary electron emission yield from a velvet surface *J. Appl. Phys.* **120** 213302
[17] Huerta C, Matlock T and Wirz R 2016 View factor modeling of sputter-deposition on micron-scale-architectured surfaces exposed to plasma *J. Appl. Phys.* **119** 113303
[18] Li G Z, Matlock T S, Goebel D M, Dodson C A, Matthes C S, Ghoniem N M and Wirz R E 2017 *In situ* plasma sputtering and angular distribution measurements for structured molybdenum surfaces *Plasma Sources Sci. Technol.* **26** 065002
[19] Matthes C S, Ghoniem N M, Li G Z, Matlock T S, Goebel D M, Dodson C A and Wirz R E 2017 Fluence-dependent sputtering yield of micro-architectured materials *Appl. Surf. Sci.* **407** 223–35
[20] Baldwin M, Doerner R, Nishijima D, Tokunaga K and Ueda Y 2009 The effects of high fluence mixed-species (deuterium, helium, beryllium) plasma interactions with tungsten *J. Nucl. Mater.* **390** 886–90
[21] Kajita S, Sakaguchi W, Ohno N, Yoshida N and Saeki T 2009 Formation process of tungsten nanostructure by the exposure to helium plasma under fusion relevant plasma conditions *Nucl. Fusion* **49** 095005
[22] De Temmerman G, Bystrov K, Zielinski J, Balden M, Matern G, Arnas C and Marot L 2012 Nanostructuring of molybdenum and tungsten surfaces by low-energy helium ions *J. Vac. Sci. Technol.* A **30** 041306
[23] Wright G, Brunner D, Baldwin M, Doerner R, Labombard B, Lipschultz B, Terry J and Whyte D 2012 Tungsten nano-tendril growth in the Alcator C-Mod divertor *Nucl. Fusion* **52** 042003
[24] Meyer F, Hijazi H, Bannister M, Unocic K, Garrison L and Parish C 2016 Flux threshold measurements of He-ion beam induced nanofuzz formation on hot tungsten surfaces *Phys. Scr.* **2016** 014019
[25] Hollmann E M, Doerner R P, Nishijima D and Pigarov A Y 2017 Observation of reduction of secondary electron emission from helium ion impact due to plasma-generated nanostructured tungsten fuzz *J. Phys. D: Appl. Phys.* **50** 445203
[26] Ye M, He Y, Hu S, Yang J, Wang R, Hu T, Peng W and Cui W 2013 Investigation into anomalous total secondary electron yield for micro-porous Ag surface under oblique incidence conditions *J. Appl. Phys.* **114** 104905
[27] Wesson J and Campbell D J 2011 *Tokamaks* vol 149 (Oxford: Oxford University Press)
[28] Tolias P 2014 On electron backscattering from dust grains in fusion plasmas *Plasma Phys. Control. Fusion* **56** 045003
[29] De Lara J, Pérez F, Alfonseca M, Galán L, Montero I, Román E and Garcia-Baquero D 2006 Multipactor prediction for on-board spacecraft RF equipment with the MEST software tool *IEEE Trans. Plasma Sci.* **34** 476–84
[30] Jonker J 1951 The angular distribution of the secondary electrons of nickel *Philips Res. Rep.* **6** 372–87
[31] El Gomati M, Walker C, Assa'd A and Zadražil M 2008 Theory experiment comparison of the electron backscattering factor from solids at low electron energy (250–5000 eV) *Scanning* **30** 2–15
[32] Andronov A, Smirnov A, Kaganovich I, Startsev E, Raitses Y and Demidov V 2013 Secondary electron emission yield in the limit of low electron energy (arXiv:1309.4658)
[33] Furman M and Pivi M 2002 Probabilistic model for the simulation of secondary electron emission *Phys. Rev. Spec. Top.* **5** 124404
[34] Seiler H 1983 Secondary electron emission in the scanning electron microscope *J. Appl. Phys.* **54** R1–18
[35] Chung M and Everhart T 1974 Simple calculation of energy distribution of low-energy secondary electrons emitted from metals under electron bombardment *J. Appl. Phys.* **45** 707–9
[36] Curren A and Jensen K 1984 Secondary electron emission characteristics of ion-textured copper and high-purity isotropic graphite surfaces *Technical Report* NASA